A fracture-propagation-control model for pipelines transporting CO_2-rich mixtures including a new method for material-model calibration

H.O. Nordhagen[b], S.T. Munkejord[a,*], M. Hammer[a], G. Gruben[b], M. Fourmeau[b], S. Dumoulin[b]

[a]SINTEF Energy Research, P.O. Box 4671 Sluppen, NO-7465 Trondheim, Norway
[b]SINTEF Materials and Chemistry, P.O. Box 4670 Sluppen, NO-7465 Trondheim, Norway

Abstract

This work considers a predictive numerical modelling approach for fracture-propagation control in CO_2-transport pipelines, an area where current engineering tools do not work. Fluid-structure interaction model simulations are compared with three published medium-scale crack-arrest experiments with CO_2-rich mixtures. The fluid flow is calculated by a one-dimensional homogeneous equilibrium model, and the thermodynamic properties of CO_2 are modelled using the Span–Wagner and the Peng–Robinson equation of state. The pipe material is represented by a finite-element model taking into account large deformations and fracture propagation. Material data commonly found in the literature for steel pipes in crack-arrest experiments is not sufficient to directly calibrate the material model used here. A novel three-step calibration procedure is proposed to fill the information gap in the material data. The resulting material model is based on J_2 plasticity and a phenomenological ductile fracture criterion. It is shown that the numerical model provides good predictions of the pressure along the pipe, the ductile fracture speed and a conservative estimate of the final crack length. An approximately plane-strain stress state ahead of crack tip implies that a fracture criterion accounting for a wide range of stress states is not necessary.

Keywords: Carbon dioxide, Finite-element method (FEM), Computational fluid dynamics (CFD), Fluid-structure, Running-ductile fracture, Pipeline, West-Jefferson, Decompression, Fracture propagation control

1. Introduction

Transport of large amounts of gases and liquids by pipeline is considered an efficient and safe method. The major part of the worldwide experience in this field is based on transport of natural gas and oil. Transport of CO_2 by pipelines – as would be needed for CO_2 Capture and Storage (CCS) to have a significant effect on global CO_2 emissions [1] – is different in many ways [see e.g. 2, 3].

Unlike natural gas transport pipelines, which are often located far from populated areas, major CO_2 emitters are commonly situated close to populated areas. Thus, a CO_2 pipeline failure with a resulting leak of asphyxiant CO_2 may have high consequences. For CCS, the CO_2 will, most likely, be transported in a liquid or dense liquid state, whereas natural gas normally is transported in a dense gaseous state. The implications of this difference are important when considering cases where an accidental rupture is caused to a pressurized pipeline – e.g. by third party impact.

In the event of pipeline failure, a rupture of sufficiently large initial size may start to propagate rapidly along the pipe. For modern-type pipeline steels, the fracture mode is ductile and the phenomenon is called a running-ductile fracture (RDF). An RDF can run over long distances – releasing a large amount of energy and dispersing CO_2 over a wide area. Though this is a very rare phenomenon, it has potentially large consequences related to economy, health and safety – and is thus a risk that needs to be carefully considered and minimized.

The severity and extent of an RDF is governed by a 'race' between the depressurization wave velocity (related to the speed of sound) in the fluid inside the pipe, and the fracture-propagation velocity. In the two-curve method (TCM)

---

for fracture propagation control (FPC) [4], the phenomenon is simplified by considering two pressure-dependent functions, one for the stable fracture velocity and one for the depressurization-wave velocity. If there exists a pressure level at the crack tip where the fracture velocity is higher than the depressurization velocity, the fracture could in principle propagate indefinitely – or until a region of higher fracture resistance is encountered.

In the COOLTRANS project [5, 6], run by National Grid (UK), results from five experiments related to FPC in dense-phase CO_2 were reported [7–9]. Two of these experiments represented full-scale crack-arrest experiments with a CO_2-N_2 mixture, and the conclusion was that the TCM, is 'not (currently) applicable to liquid or dense phase CO_2 or CO_2-rich mixtures' [9].

In codes and regulations where FPC in pipelines is considered, e.g. [10, 11], the TCM is almost exclusively used. However, with the introduction of high-grade steels (X70 and higher), the TCM has proven to become less accurate and correction factors have been introduced to achieve better predictions [12]. Recent studies show that the need for correction factors is related to new manufacturing processes for steel pipes, independent of steel grade [13]. Further, it is found that for high-toughness steel pipes, design based on Charpy tests and the TCM with correction factors is not conservative [13]. While low-toughness Charpy tests tend to be dominated by cleavage fracture, high-toughness Charpy tests usually display a fracture zone dominated by ductile fracture. The different micro-mechanical mechanisms present in the Charpy tests of low-toughness and high-toughness materials are likely to reflect the behaviour of the RDF in full scale pipelines. Leis [14] pointed out that for modern high-toughness steel pipes, the running fracture is more a propagating local instability than an extending crack.

Unlike lean natural gas, dense-phase CO_2 will undergo a phase transition upon depressurization and will sustain a high pressure (crack-driving force) on a propagating fracture [2, 3, 15]. This is due to a drop in pressure-propagation speed (below the typical fracture speed) in the two-phase region, and a high-enough saturation pressure to propagate the fracture [8, 15]. In [3] we found that the forces on the opening fracture flaps are significantly more severe for CO_2 than for natural gas pipelines. For an RDF in a natural-gas pipeline, the crack-driving force falls to negligible levels at about 1 pipe diameter (D) behind the moving crack tip [16], whereas for CO_2 a high pressure level is maintained even at 4–5D away from the crack tip [3]. In addition, depending on the capture technology, the level and type of impurities will vary [17], and this may significantly alter the thermophysical properties [18] and therefore the magnitude of the crack-driving forces.

This highlights the need for further development of design tools for pipelines. Several approaches to predict and understand the RDF problem in pipelines have been developed over the years [3, 19–26]. Recently, a fluid-structure model for brittle fracture in pipelines was presented [27], as brittle fracture may be relevant e.g. due to the cooling around a leak.

In [3, 28, 29] we presented a numerical methodology for FPC aiming to include the important physics, with reasonable computational cost. In this way we aim to establish a tool for safe (with respect to FPC) and cost-effective design and operation of CO_2 pipelines. The method consists of two main parts: a one-dimensional CFD model accounting for the fluid flow inside and out of the pipe, and a finite-element model accounting for the non-linear mechanical behaviour of the pipe wall and the crack propagation. A fluid-structure interaction coupling scheme between these two parts is implemented. This coupled fluid-structure model has been validated against crack-arrest experiments performed with methane and hydrogen [28, 29] and it has been extended to accurately account for two-phase (gas-liquid) and three-phase (gas-liquid-solid) CO_2 [3, 19, 30–32]. Furthermore, an improved method to estimate the circumferentially varying pressure load on the fracture flaps has been developed, and a backfill model has been employed to represent the material surrounding the pipe [3].

In [3], two medium-scale fracture propagation tests done in the CO2PIPETRANS project, with pure CO_2 in the dense phase, were compared with results from the new methodology. Good agreement in terms of fracture velocity, final fracture length and pressure data of the method was obtained. The simulation results also provided possible explanations to why the existing empirical models fail to give an estimate of the arrest/no-arrest boundary as reported in e.g. [9] for CO_2 transporting pipelines. Thus, since the TCM was developed using low-toughness materials and ideal gases, the fracture velocity curve and the crack arrest conditions for CO_2 pipelines most likely need to be revised [3, 9].

In the present work, we consider the COOLTRANS experiments [7–9] for model validation. These experiments differ in several ways from those so far used to validate the new methodology [3]. Firstly, the pipe outer diameter and wall thickness used in [7–9] were 914 mm and 25.4 mm, respectively (compared to 406 mm and 6–8 mm, respectively, in [3]). In three of the five reported experiments in [7–9], a CO_2-rich mixture was used, compared to the pure CO_2

Table 1: Summary of the West-Jefferson tests reported in [8]. Cr.len denotes the final crack length, from the end of the initial crack, before ring-off in each direction West/East. Init.cr.len denotes the length of the initial crack made by the explosive cutter. v_f is the average fracture velocity. Sat. pressure refers to the predicted saturation pressure after isentropic decompression from the initial state, using the equation of state for combustion gases (EOS-CG) [33].

Test	Length/#sections	Init. cr.len	Fluid composition	Pressure/temp.	Cr.len W/E	Sat. pressure	v_f (m/s)
1	16.16 m / 1	0.7 m	100% CO_2	149.2 bar/16.8 °C	1.0 m/1.0 m	41.9 bar	< 75
2	16.97 m / 2	3.0 m	100% CO_2	151.9 bar/8.2 °C	1.3 m/1.3 m	34.4 bar	< 75
3	22.71 m / 3	1.8 m	87.5% CO_2/12.5% N_2	150.0 bar/15.2 °C	6.8 m/7.1 m	93.2 bar	135–195

Table 2: Average yield stress, s_y, ultimate stress, s_u, and Charpy V-notch energies, 1/1 CVN, for the pipes used in the W-J tests [8]. Tensile testing was done at ambient temperature and Charpy testing at 0 °C. The material IDs used here are chosen for convenience. According to [8], the corresponding pipe numbers were MAT1 = 3553, MAT2 = 44993, MAT3 = 33992, MAT4 = 33S, MAT5 = 33N, MAT6 = 55.

Test	Material ID	s_y (MPa)	s_u (MPa)	CVN (J)
1	MAT1	533.3	610.7	201
2	MAT2	491.0	582.2	184
	MAT3	511.0	589.0	194
3	MAT4	515.0	633.0	199
	MAT5	534.5	643.5	193
	MAT6	458.0	552.0	342

used in [3]. Moreover, the available material data for the steel pipes from the experiments of [7–9] are restricted to the yield and ultimate stress as well as the fully ductile Charpy V-notch energy. This constitutes a challenge for properly calibrating the material and fracture parameters used in the presented finite-element model. This challenge is addressed here. In doing so, we attempt to put the uncertainties on the conservative side.

The rest of this paper is organized as follows: An overview of the crack-arrest experiments considered here is described in Section 2, while Section 3 presents the coupled fluid-structure model and a new method for calibration of the pipe material models. In Section 4, results from numerical simulations are presented, discussed and compared with the experimental data. Conclusions are drawn in Section 5.

2. Reference crack-arrest experiments

In the COOLTRANS [5] project, challenges related to fracture-propagation control (FPC) in pipelines transporting CO_2 rich mixtures were investigated. Three reduced-length tests, also known as West-Jefferson (W-J) tests [8], and two full-scale fracture-propagation tests [9] with CO_2-rich mixtures have been reported. The three W-J tests are considered here, and a summary of the experimental details and the main results are given in Table 1. The W-J tests were conducted primarily to show whether and how an initial defect in a modern-type steel pipeline carrying CO_2-rich mixtures will propagate as a running-ductile fracture (RDF) [8]. It was also investigated how large an initial defect would have to be to develop into a running ductile fracture, and whether this could actually take place in a large-diameter and -thickness high-toughness modern pipeline steel grade. In the following, we will briefly describe the layout and essential details of the three W-J tests. More information can be found in [8].

The pipes were made of Grade L450 steel and had an outer diameter of 914 mm (36 inch) and a 25.4 mm wall thickness. The Grade L450 is under API considered equivalent to the X65 grade pipeline steel. The reported yield stress (yield strength) and ultimate stress (tensile strength) of the L450 grades used are shown in Table 2[1]. These values were significantly different from those of the X65 steel considered in our recent work on pure CO_2 [3].

The test layout for the three W-J tests is shown schematically in Figure 1 and is based on information given in [8]. One 16.6 m long pipe, with material defined as MAT1 in Table 2, was used in Test 1. In Test 2, two pipes, each

---

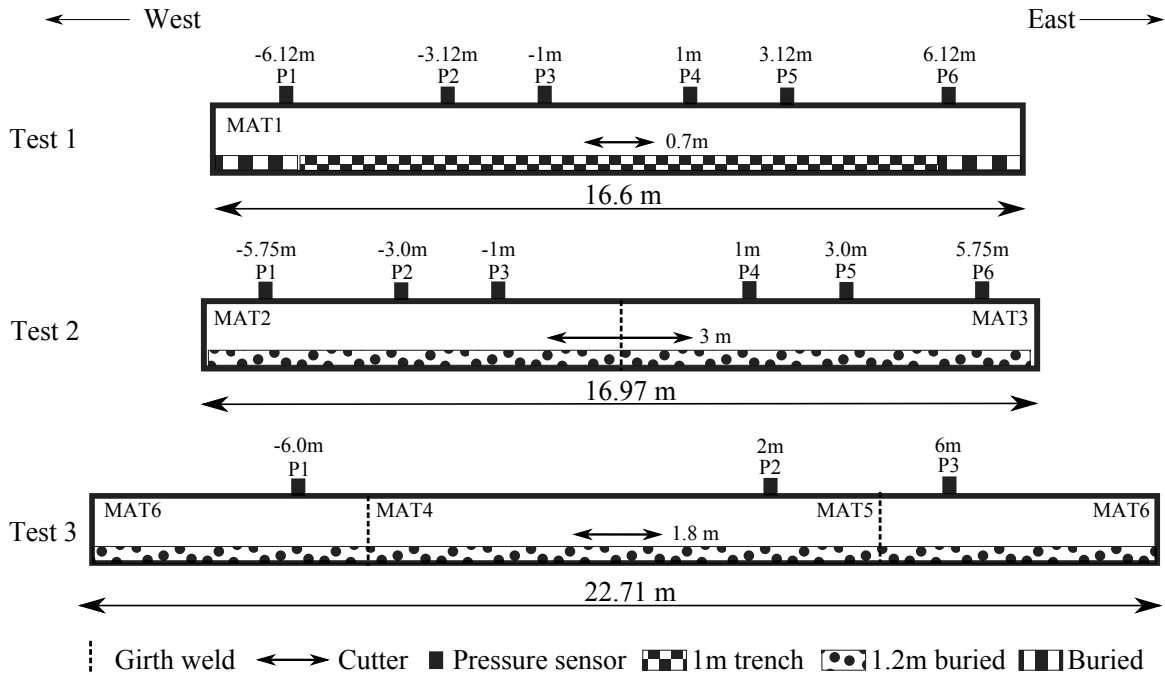[1]The yield stress and the ultimate stress values for MAT6 are taken from [34].

Figure 1: Layout of the W-J tests reported in [8]. Pressure transducers (denoted P#) were mounted at 3 o'clock positions. Numbers above these indicate distance from the initial crack tip. The different backfill conditions are noted in various shaded boxes. Material grades MAT1–MAT6 are defined in Table 2. Total pipe length (excluding domes welded at the end) and initial crack lengths are indicated with arrows.

about 8.5 m long and with materials defined as MAT2 and MAT3 in Table 2, were used. Test 3 consisted of three pipe segments: one 8.5 m long pipe segment with materials defined as MAT4 and MAT5 (measured at each end of the pipe), and two high-toughness outer pipe sections (defined as MAT6) – each 5.96 m long and coming from the same original pipe (Pipe No. 55). Domed end caps were welded to the ends of each test (not part of total length). Shaped explosive charges with lengths given in Table 1 – shown with arrows in Figure 1 – ensured the initial through-wall crack lengths at the start of each test.

Pressure transducers, positioned as indicated in Figure 1, recorded the pressure during the tests. Timing wires for measuring the fracture speed were mounted along the pipes. Careful monitoring and stabilization of the initial temperature and pressure (indicated in Table 1) in tests were performed. Logging of data failed for pressure sensor P5 in Test 1, and sensors P2 and P3 in Test 2. No information of the state and type of the backfill is given in [8].

The final propagated crack lengths prior to ring off are given in Table 1. Results from the two first W-J tests with pure CO_2 resulted in short crack lengths – as was expected due to the relatively low saturation pressure and high toughness and thickness of the pipes. The running ductile fracture in Test 3 was driven by a high saturation pressure and arrested in the high toughness reservoir pipe (MAT6) in each direction of propagation. However, the arrest may have been affected by the reflected pressure wave. Thus, the only conclusion regarding the toughness needed for crack arrest in Test 3 is that it must be equal to, or larger than, approximately 200 J. While Test 1 and 2 arrested through a ring-off mechanism, Test 3 arrested as a straight fracture.

3. The numerical model

This section summarizes the coupled numerical model which takes into account the fluid-structure interaction between the pipe and the CO_2 as well as the interaction between the pipe and the backfill. A more detailed description of the model can be found in [3].

The coupled model consists of two main parts: a structure model taking into account deformation and fracture of the pipe material and the surrounding (backfill) material, and a fluid-dynamic model accounting for the fluid behaviour. The structure model passes the fracture opening and pipe geometry to the fluid-dynamic model, which then calculates the flow through the fracture and the pressure field along the pipe axis. Next, this pressure field is passed to the structural model and applied to the finite elements.

3.1. Structure model

The pipeline was modelled by the nonlinear finite-element (FE) code LS-DYNA [35], following the same approach as in [3]. In the simulations, the pipe was loaded to the initial pressure using an implicit time-integration scheme, followed by an RDF step which used an explicit time integration scheme. As in [29], Belytschko-Tsay shell elements with one in-plane integration point and 5 integration points through the thickness were applied in the discretization of the pipe. As discussed in [36] and [3], a local neck having a width approximately equal to the pipe thickness, is travelling ahead of the RDF. Most of the plastic energy is dissipated in the necking region [16, 37], thus the pipe thickness is taken as the significant length scale in the RDF simulations. As will be shown in Section 4.3, the pipe thickness at the crack-tip is reduced during plastic deformation, while undergoing a state of plane-strain in the longitudinal direction of the pipe. An applied element size of approximately 25 mm along the crack-path direction and 12.5 mm in the in-plane transverse direction was found appropriate. The elements outside the crack path were not exposed to similarly large strains, and were given an initial element size of approximately 25 mm with an aspect ratio close to unity. The model of Test 1 consisted of 35000 shell elements, while the models of Test 2 and 3 had 37000 and 49000 shell elements, respectively.

3.1.1. Steel pipe material model

The constitutive model for the steel-pipe material – which is similar to the one used in [3] – was described by a hypoelastic, visco-plastic material model. The elastic properties are described by a Young's modulus of 208 GPa and a Poisson ratio of 0.3. The dynamic yield function, f, is based on the J_2 flow theory and is expressed as

$$f(\boldsymbol{\sigma}) = \sigma_{VM}(\boldsymbol{\sigma}) - \sigma_f(p, \dot{p}) \tag{1}$$

where $\sigma_{VM} = \sqrt{\frac{3}{2}\boldsymbol{\sigma}:\boldsymbol{\sigma}}$ is the von Mises equivalent stress, $\boldsymbol{\sigma}$ is the Cauchy stress tensor, p is the equivalent plastic strain, $\dot{p}$ is the equivalent plastic strain rate and σ_f is the flow stress. The flow stress is modelled with a work-hardening based on the two-term Voce equation [38] with a multiplicative visco-plasticity part as in [39], and is expressed as

$$\sigma_f = \left[\sigma_0 + \sum_{i=1}^{2} Q_i \left(1 - \exp\left(-\frac{\theta_i}{Q_i}p\right)\right)\right]\left(1 + \frac{\dot{p}}{\dot{p}_0}\right)^C. \tag{2}$$

Herein, σ_0 is the yield stress, θ_i are the initial hardening moduli, Q_i are the hardening saturation values, while $\dot{p}_0$ and C are parameters controlling the strain-rate sensitivity.

The steel pipes fractured in a slant through-thickness mode running at 75–200 m s^{-1} [8]. This fracture mode is a result of shear-banding which occurs over a length scale of 10–100 μm and cannot be captured in a numerical model unless a very dense mesh is applied in combination with material softening [40, 41]. However, previous studies indicate that a good engineering representation of the fracture resistance can be achieved as long as the local necking is properly captured in the numerical model [36, 42]. In this study, fracture propagation is modelled by means of the element deletion method; as a fracture criterion is met in one integration point, the element lose its load-carrying capacity. The RDF is thus modelled as a sequence of fracture initiations in the eroded elements. To predict fracture initiation, the Cockcroft-Latham (CL) ductile-fracture criterion [43] is applied. The CL fracture criterion predicts onset of fracture when the major principal stress integrated over the equivalent plastic strain path reaches a critical value, i.e.

$$W_c = \int_0^{p_f} \langle\sigma_I\rangle \mathrm{d}p, \quad \langle\sigma_I\rangle = \max(\sigma_I, 0). \tag{3}$$

Here σ_I is the major principal stress, p_f is the equivalent plastic strain at fracture and W_c is a material parameter.

3.1.2. Calibration of material model for test pipelines

The material parameters used in the material model, defined by Eqs. (1)–(3), are usually calibrated from a set of quasi-static and dynamic tensile tests. For more details on the calibration procedure, see e.g. [29]. However, the information available about the steel materials in the experiments considered here is limited to the yield stress, the ultimate tensile stress and the Charpy V-notch values [8], see Table 2. These parameters are the ones customarily reported from RDF experiments, but they are not sufficient for a straightforward calibration of the material model used here. Thus, a three step process was established in order to carry out the calibration based on the limited material data set:

1. Determine the two parameters of a power-law work hardening model from the reported yield and ultimate stresses, by employing the empirical methods presented by Liessem et al. [44] and Lu et al. [45], and then fit the Voce model (Eq. (2)) to the power-law work hardening model.
2. Determine the CL fracture parameter for solid elements by inverse modelling of the Charpy test.
3. Establish the fracture parameter for shell elements with the relevant length scale from simulations of a virtual tensile test.

Since the method for establishing work hardening [44, 45] does not account for viscoplasticity, the strain-rate parameters were assumed to be the same as the ones presented for an X65 material [29], i.e. C=0.015 and $\dot{p}_0 = 0.011\,\mathrm{s}^{-1}$. It is emphasized that step 1 in the calibration process is related to the work hardening of the material, while step 2 and step 3 are related to the ductile fracture modelling of the material. The ductile fracture model is first calibrated for small-sized (0.3 mm) solid elements in step 2, since shell elements are not able to properly capture the geometry of the small-sized Charpy specimen. However, the material model is to be used in simulations of steel pipes which are discretized by relatively large (25 mm) shell elements, thus step 3 is introduced in order to transfer the calibrated fracture parameter from a small length scale to a larger length scale. In the following, details of the three steps in the calibration process are given.

Work hardening. Following [44], we can express the flow stress (σ_f) and work hardening of the steel pipe material by the Hollomon equation as

$$\sigma_f = Ap^n, \tag{4}$$

where A and n are the parameters to be calibrated. Based on the empirical relationships given by Liessem et al. [44] for X56, X60, X65, X70 and X100 steels, n can be estimated from the engineering yield stress, s_y, and the engineering ultimate stress, s_u, as

$$\frac{s_u}{s_y} = (1 + e_y)\left(\frac{n}{\tilde{e}e_y}\right)^n. \tag{5}$$

Here $\tilde{e}$ is the Euler number and e_y is the engineering strain at yielding. Lu et al. [45] found that by letting $e_y = 0.005$, an explicit expression of n can be obtained by approximating Eq. (5) as

$$n = \sum_{i=1}^{2} a_i \left[\ln\left(2 - \frac{s_y}{s_u}\right)\right]^{b_i}, \tag{6}$$

where $a_1 = 0.1507$, $a_2 = 0.5745$, $b_1 = 0.4607$ and $b_2 = 1.6099$. When n is determined from Eq. (6), the Hollomon coefficient, A, can be calculated as [45]

$$A = s_u \left(\frac{\tilde{e}}{n}\right)^n. \tag{7}$$

The resulting Hollomon work hardening parameters for the materials in the present study are given in Table 3. Since the flow stress in our numerical model is based on Eq. (2), a least-squares minimization was conducted to find the yield stress σ_0, and the Voce work hardening parameters, θ_i and Q_i. The reference curve for the minimization was the derived Hollomon work hardening curve in the interval $0 < p < 1.5$, and a constraint was included so that the Voce and Hollomon work hardening curves predicted the same strain at diffuse necking ($p = n$). The resulting yield stress and Voce work hardening values are presented in Table 3, while Figure 2a shows that the Hollomon and Voce models are coherent in predicting the true stress-strain curves. It can be seen from Figure 2a that MAT4 and MAT5 display a higher level of flow stress than MAT1–MAT3, which again display a somewhat higher flow stress than MAT6.

Table 3: Hollomon and Voce work hardening parameters for steel pipe materials.

Test	Mat. ID	A (MPa)	n (−)	σ_0 (MPa)	θ_1 (MPa)	Q_1 (MPa)	θ_2 (MPa)	Q_2 (MPa)
1	MAT1	800.1	0.076	539.0	3130.6	119.8	280.3	175.5
2	MAT2	787.0	0.088	498.2	3159.4	132.7	300.7	198.5
	MAT3	776.4	0.078	516.5	3065.5	119.4	277.1	175.2
3	MAT4	881.2	0.100	526.1	3563.4	162.2	362.6	250.6
	MAT5	881.0	0.093	544.7	3525.2	154.0	347.0	234.2
	MAT6	753.3	0.094	465.3	3071.0	133.7	299.9	202.1
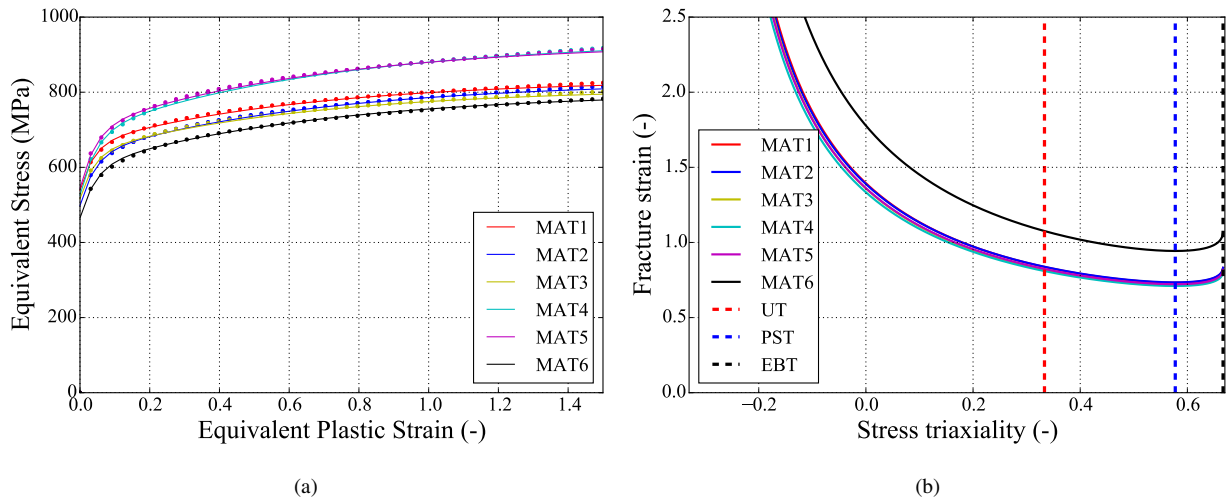
Figure 2: (a) Predicted work hardening for MAT1–MAT6. The lines represent the Voce model, while the dots represent the Hollomon model. (b) The plane-stress Cockcroft-Latham fracture loci as calibrated for shell elements in the σ^*–p_f space. The stress states corresponding to uniaxial tension (UT), plane-strain tension (PST) and equi-biaxial tension (EBT) are marked with dashed lines.

Table 4: Cockcroft-Latham fracture parameter for solid (W_c^{solid}) and shell elements (W_c^{shell}) (MPa).

Material	MAT1	MAT2	MAT3	MAT4	MAT5	MAT6
W_c^{solid}	1210	1105	1150	1220	1155	1825
W_c^{shell}	614	579	597	652	635	746

Fracture model for solid elements. The CL fracture parameter for solid elements, W_c^{solid}, for each of the six materials, was identified from simulations of the Charpy test. None of the experimentally obtained Charpy tests experienced complete fracture [8], thus the CVN values in Table 2 are influenced by energy dissipated due to friction between the Charpy specimen and the testing apparatus. Cosham et al. [8] reported that 100% of the fracture zone in all Charpy tests was of a shear type, i.e., the fracture occurred due to microvoid nucleation, growth and coalescence and not brittle cleavage. This implies that plastic deformation during the Charpy tests took place in a large region of the specimen, thus a ductile fracture criterion is appropriate in terms of fracture modelling of the Charpy tests. The finite-element models of the Charpy tests were based on the in-plane geometry shown in Figure 3a and a full size Charpy specimen thickness of 10 mm. In order to reduce the computational time in the numerical models, two symmetry planes were applied; one in the thickness direction and one in the longitudinal direction of the specimen as indicated in Figure 3b. The specimen was supported by a cylinder (green part in Figure 3b) with a diameter of 2.5 mm, while the striker had a cylindrical shape with a diameter of 6.4 mm (blue part in Figure 3b). The striker impacted the sample at its centre with a velocity of 5.5 m/s. The mass of the striker was adjusted so that the impacting energy of the striker was equal to the impact energy in the corresponding Charpy experiments, that is 300 J for MAT1–MAT3, and 750 J for MAT4–MAT6 [8]. The simulations of the Charpy tests were run in the explicit solver of LS-DYNA [35], with the viscoplastic constitutive model presented in Section 3.1.1 and the Voce work hardening parameters from Table 3. A rigid body formulation was used for the material of the striker and the support. The specimen, the support and the striker were discretized by hexahedral elements (LS-DYNA type −1), and the characteristic element size in the region where fracture occurred was 0.3 mm. Fracture was included by the element erosion technique based on the CL fracture criterion. The support-specimen and the striker-specimen contact had a surface-to-surface formulation with a Coulomb static friction coefficient of 0.60. The friction had an exponential decay for increasing relative velocity between the contact surfaces, which saturated at a dynamic friction coefficient of 0.18. The exponential decay coefficient was set to 0.023. The parameters in the friction model were determined from experimental tests carried out at different sliding velocities between a X65 steel and a steel of similar hardness as the striker. The only parameter that was varied in the inverse modelling process for each material was W_c^{solid}. For each material, the inverse modelling process was stopped when the numerical Charpy V-notch value differed less than 1 J from the experimental value in Table 2. As in the experiments, none of the Charpy simulations experienced complete fracture. Notably, the Charpy simulations with MAT1–MAT5 displayed a larger sensitivity to W_c^{solid} than MAT6. This may be a result of the relatively large amount of energy dissipated through friction in the Charpy test of MAT6. In conclusion, the inverse modelling method for calibrating the ductile fracture criterion from simulated Charpy tests, is likely to be more accurate for the materials MAT1–MAT5 than for the very-high-toughness material MAT6. The resulting values of W_c^{solid} are given in Table 4, while Figure 3c shows the force-displacement curves from the Charpy test simulations.

A validation based on the force-displacement curves from the Charpy test reported in [8] is not possible as these tests were only instrumented for measuring energy absorption. However, Cosham et al. [46] presented force-displacement curves from Charpy tests conducted on similar materials. Experimental force-displacement curves from tests having CVN values of 148 J, 238 J and 338 J (taken from Figure 3 in [46]) are given in Figure 3c together with the simulated force-displacement curves from the present study. As shown, the simulated force-displacement curves for MAT1-MAT5 (having CVN values between 184 J and 201 J) fall between the selected experimental curves with CVN values of 148 J and 238 J, while the simulated curve for MAT6 (with CVN equal to 342 J) agrees well with the experimental curve having a CVN value of 338 J. The results indicate that the simulated Charpy tests are representative.

Fracture model for shell elements. In order to establish a fracture parameter corresponding to the relevant length scales in the RDF simulations, a set of simulations of quasi-static uniaxial tension tests was carried out. These simulations were conducted with the implicit solver Abaqus/Standard v6.14 [47] applying the visco-plastic hardening
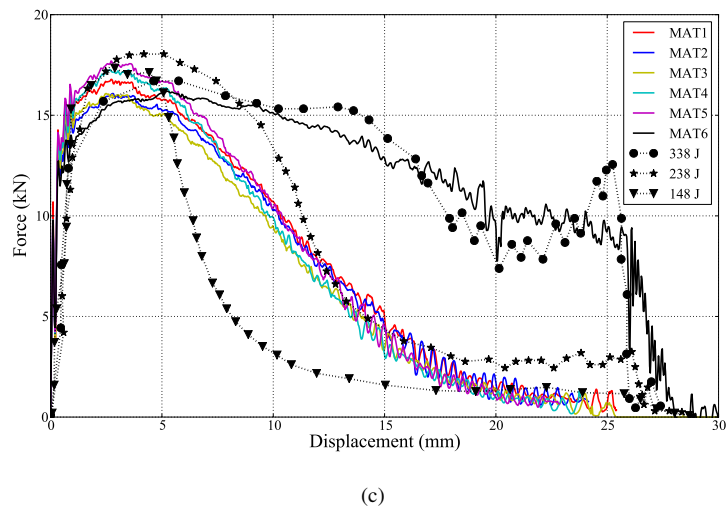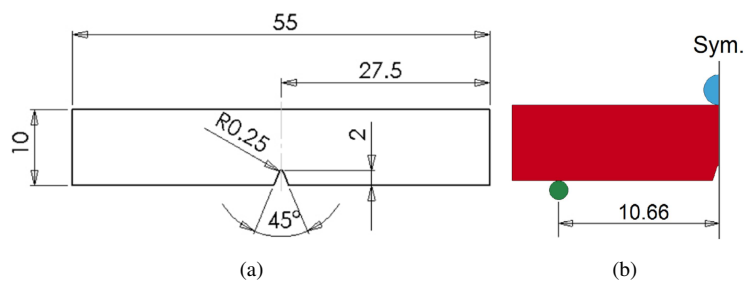
Figure 3: (a) In-plane geometry of numerical Charpy model, (b) boundary conditions of numerical Charpy model, and (c) force-displacement curves from the simulated Charpy tests and three curves from experimental Charpy tests taken from [46] (the total absorbed energy in the experimental curves is noted in the legend).
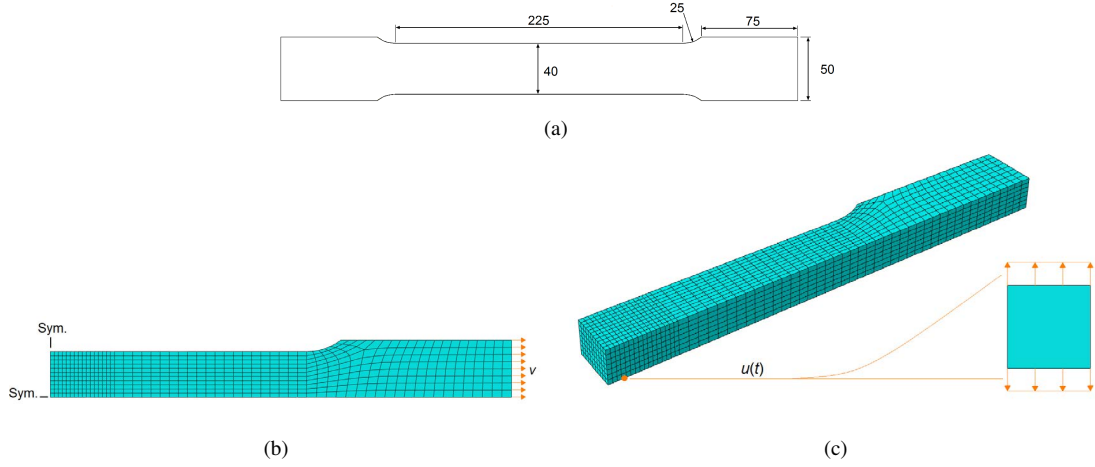
Figure 4: Virtual uniaxial tensile test. (a) In-plane geometry, (b) in-plane mesh, in-plane symmetry planes and prescribed loading and (c) position where the displacement was collected for single-shell-element simulation.

model presented in Section 3.1.1 with the Voce hardening parameters from Table 3 and the W_c^{solid} values from Table 4. The geometry of the tensile test was adopted from ASTM E8/E8M-15. One quarter of the in-plane geometry is shown in Figure 4a. The thickness of the specimen was set to 25.4 mm. Three symmetry planes were used in the numerical model. Two of these are shown in Figure 4b while the third is in the through-thickness direction. A prescribed velocity $v = 0.225\,\mathrm{mm\,s^{-1}}$ was applied on the nodes at the end of the specimen, see Figure 4b. This loading gave a strain rate of $0.002\,\mathrm{s^{-1}}$ before necking in the gauge zone. The region exposed to necking was discretized with selectively reduced hexahedral elements. Seven solid elements were used in the thickness direction and the elements had a near cubic shape in the region exposed to diffuse necking. The time at onset of fracture, t_f was defined as the instant when W_c^{solid} occurred in one Gauss point. For each material, a second simulation was conducted on an initially square shell element with initial side lengths of 12.5 mm and initial thickness of 25.4 mm. The shell element model had the same plasticity formulation as their corresponding solid element models. The displacement, $u(t)$ for $0 \leq t \leq t_f$, of a point positioned initially 6.25 mm in the longitudinal direction from the centre of each solid element model was collected and applied to produce a uniaxial loading in the corresponding shell element model, see Figure 4c. From the shell element model a new value W_c^{shell} was established by conducting the integration in Eq. (3). The W_c^{shell} values that were obtained – and that were later used as fracture criterion in the coupled simulations – are shown in Table 4.

3.1.3. Ductile fracture and the Cockcroft-Latham criterion

Ductile fracture is the result of nucleation, growth and coalescence of microvoids during plastic deformation, [48, 49]. For increased levels of pressure, the growth of microvoids inside the material is detained. This results in increased material ductility and the material can undergo larger plastic deformation before a new fracture surface is created. The pressure acting on the material can be expressed by the stress triaxiality, σ^*, which is defined as

$$\sigma^* = \frac{\sigma_m}{\sigma_{VM}}, \tag{8}$$

where $\sigma_m = \mathrm{tr}\,\boldsymbol{\sigma}/3$ is the mean stress. Over the last decade, increased attention has been given to the effect of the deviatoric stress state on the ductility of metallic materials in the range of low stress triaxiality $\sigma^* < 1$, e.g. [50–52]. For instance, many steels display higher ductility in equi-biaxial tension ($\sigma^* = 2/3$) than in plane-strain tension ($\sigma^* = \sqrt{3}/3$), see e.g. [53–55]. The increased ductility with higher triaxiality, as seen when comparing plane-strain with equi-biaxial tension, may be attributed to the difference in the deviatoric stress state, which can be represented by the Lode parameter, μ. The Lode parameter gives a normalized measure of the position of the intermediate principal stress between the major and minor stresses, and is expressed as

$$\mu = \frac{2\sigma_{II} - \sigma_I - \sigma_{III}}{\sigma_I - \sigma_{III}}, \tag{9}$$

10

where $\sigma_I \geq \sigma_{II} \geq \sigma_{III}$ are the ordered principal stresses.

The material ductility, p_f, as estimated by the Cockcroft-Latham criterion, can be expressed explicitly as a function of the stress state. In order to derive such an expression, a relation between σ_{VM} and σ_I must be established. One possibility is

$$\sigma_I = \left(\frac{\sigma^* \sqrt{3 + \mu^2} + 3 - \mu}{3 \sqrt{3 + \mu^2}} \right) \sigma_{VM}. \tag{10}$$

By invoking a strain-rate sensitive Hollomon hardening law, i.e.

$$\sigma_f = A p^n \left(1 + \frac{\dot{p}}{\dot{p}_0} \right)^C, \tag{11}$$

and assuming proportional loading, we can explicitly express the influence of the stress measures σ^* and μ, as well as the strain rate $\dot{p}$, on the CL fracture criterion by combining Eqs. (3), (10) and (11) as

$$p_f = \left(\frac{W_c}{A} \frac{3 \sqrt{3 + \mu^2}}{\sigma^* \sqrt{3 + \mu^2} + 3 - \mu} \frac{n + 1}{(1 + \dot{p}/\dot{p}_0)^C} \right)^{\frac{1}{n+1}}. \tag{12}$$

In the case of plane stress, which is the case for shell elements, a one-to-one relation exists between σ^* and μ [55], thus p_f can be expressed as a function of σ^* (or μ) alone. Figure 2b visualizes the Cockcroft-Latham fracture criterion as calibrated for shell elements in the σ^*–p_f space following Eq. (12) under quasi-static loading ($\dot{p} = 0.001 \, \text{s}^{-1}$). Notably MAT1–MAT5 display an almost identical ductility while MAT6 displays a more ductile behaviour. This is in accordance with the experimentally measured Charpy V-notch values for the materials in Table 2. As can be seen from Figure 2b, the CL criterion predicts a lower ductility in plane-strain tension (PST) than in uniaxial tension (UT) and equi-biaxial tension (EBT). For compression stress states ($\sigma^* < 0$), the ductility increases and eventually approaches infinity at $\sigma^* = -1/3$.

3.2. Fluid model

3.2.1. Flow model

The fluid flow inside the pipe and out of the pipe is described using a homogeneous equilibrium model (HEM). Herein, the flow is assumed to be one-dimensional and in kinetic, mechanical, thermal and chemical equilibrium. The flow model is solved by an explicit finite-volume scheme using a Courant-Friedrich-Lewy (CFL) condition for compressible flow with a CFL number of 0.9. Details may be found in [3].

In fact, the current flow model can be regarded as two coupled 1D flow models: one along the pipe and one out of the pipe in the radial direction. In each pipe cross section, the pressure load on the pipe is estimated taking the shape of the opening pipe flaps into consideration, in effect being a quasi 2D model. The fluid-structure interaction scheme is further addressed in Section 3.3.

3.2.2. Thermodynamics

Pure CO_2. Test 1 and 2 are conducted with pure CO_2, and the Span–Wagner EOS [56] is the best suited model under the full equilibrium assumption. To solve the energy–density flash stemming from the flow equations, the approach of Giljarhus *et al.* [30] and Hammer *et al.* [31] is applied.

CO_2–N_2 mixture. In order to describe the Test 3 mixture containing 87.5 % CO_2 and 12.5 % N_2, the Peng–Robinson EOS [57] is used to model vapour and liquid phases. The approach for solving the energy–density flash is described in [58]. For the following coupled-model calculations, the appearance of solid phases is ignored.

It is possible to extend the fluid description with an auxillary model for dry ice, the Gibbs free energy model of Jäger and Span [59]. With this approach, the full phase behaviour is seen in Figure 5. The figures show the different phase regions, and the solid–liquid–vapour co-exsistence line in the temperature–pressure space. In the entropy–pressure space, the co-exsistence line becomes an area. Two critical points are also seen.

Figure 6 shows the ideal full-bore depressurization behaviour from the Test 3 conditions. The saturation pressure is predicted to be 90.0 bar. From the depressurization velocity plotted in Figure 6b, it can be seen that the fluid chokes at about 43.5 bar.
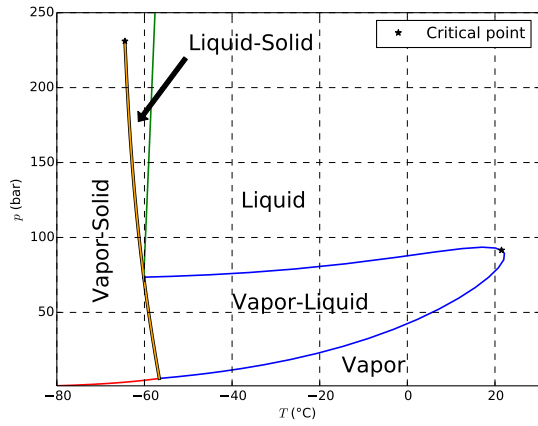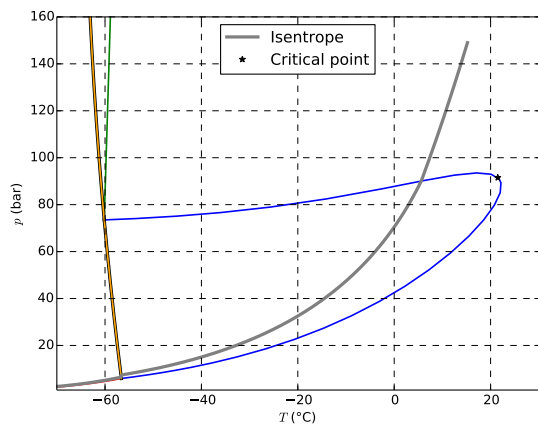
(a) Phase diagram in temperature–pressure space.
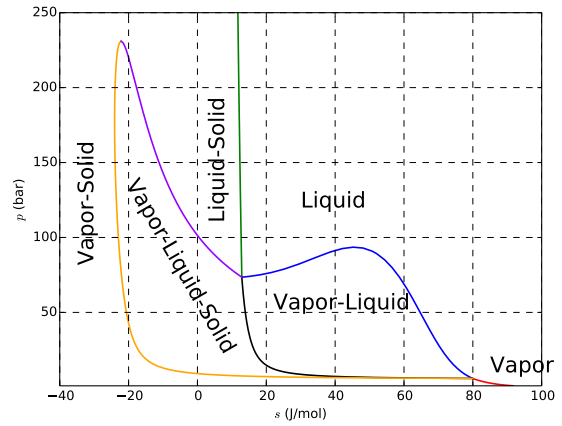
(b) Phase diagram in entropy–pressure space.

Figure 5: Phase diagrams for the 87.5 % CO_2–12.5 % N_2 mixture. The Peng-Robinson EOS is used to model the fluid phases, and the Gibbs free energy model of Jäger and Span [59] is used to model dry ice. Two critical points are present.

(a) Ideal depressurization path plotted together with the phase diagram.
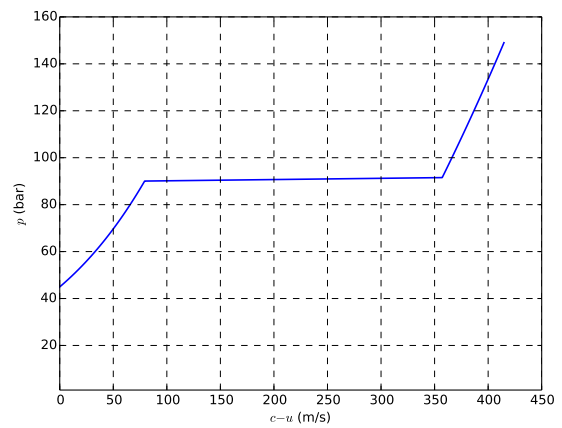
(b) Ideal depressurization velocity.

Figure 6: Ideal depressurization behaviour plotted for the 87.5 % CO_2–12.5 % N_2 mixture. The Peng-Robinson EOS is used to model the fluid phases, and the Gibbs free energy model of Jäger and Span [59] is used to model dry ice.

12

In general, different impurities may give different phase envelopes and hence equilibrium pressures, and also different speeds of sound, densities, etc. Hence the whole flow field and load on the pipe will vary with varying CO_2-mixture composition. As an illustration, in [58], different mixture compositions were considered for the case of a full-bore rupture of a pipe (but no propagating fracture).

3.3. The fluid-structure coupling

A running-ductile fracture in a pipeline represents a problem where the boundary conditions for the fluid flow depend on the structure, and the response of the structure and crack-driving force are determined by the fluid behaviour. A detailed description of the fluid-structure interactio (FSI) coupling scheme used in the model is presented in [3], and a brief overview of the method will be given in the following.

The equations governing the fluid flow and the response of the structure are treated as two computational fields and solved separately. The coupling between the solved equations are used explicitly to communicate information between the fluid and structure solutions. This is called a *partitioned approach* to FSI [60]. A non-conforming mesh method is applied. In this way, meshes that do not overlap can be employed. However, in all simulations presented here the number of fluid cells and elements in the axial pipe direction are equal.

In several studies, a strong circumferential variation in the pressure on the opening fracture flaps have been found [23, 61–63]. O'Donoghue et al. [61] observed more than 50% reduction in pressure from the bottom of the pipe to the top of the pipe just 2 to 5 ms after the RDF had passed the axial location of the pressure sensors. Since the pressure from the CO_2 acting on the flaring pipe walls is the main crack-driving force for the RDF, it is important that the circumferential variation of the pressure is represented in a proper way. The one-dimensional fluid model calculates two pressures at each axial computational cell: the cross-sectional average pressure p, and the escape pressure p_e. The latter represents the pressure at the opening. For the fluid behaviour ahead of the propagating crack tip, where no circumferential variation in pressure is observed experimentally [61–63], the average pressure, p, is applied to all elements corresponding to each fluid computational cell in the structure model. Behind the crack tip, we model the circumferential pressure variation using a pressure-profile reconstruction as described in [3], based on the assumption of quasi-steady isentropic compressible Bernoulli flow. This reconstructed pressure provides an improved load estimate with respect to the cross-sectional average pressure.

In addition to the forces exerted on the pipe by the internal fluid, external forces from the backfill will act on the pipe and absorb kinetic energy from the rapidly opening pipe. Interaction will also take place between the escaping fluid and the backfill, but this is not included in the model.

3.4. The structure-backfill coupling and backfill representation

When pipelines are buried in soil [16, 64, 65] or surrounded by water [66, 67], the presence of backfill slows down the speed of the RDF and decreases the required ductility of the steel to arrest the fracture [66, 67]. In [3] a brief review of backfill effects on RDF was given. In the following, a description of the modelling approach for backfill is presented.

In this paper, we have chosen to represent backfill using the smoothed particle hydrodynamics (SPH) method. SPH is a mesh-free Lagrangian method, that is well suited to describe granular materials under large deformations, see [68]. The backfill was discretized by SPH particles with a nodal distance of 100 mm. Test 1 was trenched to a depth of 1.0 m apart from the last 1.0 m at the boundary which was fully buried, while Tests 2 and 3 were fully buried. An illustration of the backfill geometry is shown in Figure 7. The model of Test 1 had 182000 SPH particles, while the models of Tests 2 and 3 had 206000 and 277000 SPH particles, respectively. The contact between the SPH particles and the pipeline shell elements was modelled with a node-to-surface method, and a velocity independent coefficient of friction of 0.4. A soft constraint formulation, with a scale factor of 0.1 for the constraint forces during contact, was used. With the soft constraint option, the interface stiffness is based on the nodal mass and the global time step size.

From interpretation of the pictures in [8], the backfill materials in Tests 1 and 3 were assumed to be clay, while the backfill material in Test 2 was assumed to be silt. The plastic behaviour of the backfill materials was described by the Mohr–Coulomb (MC) model. The yield surface of the MC model is given by

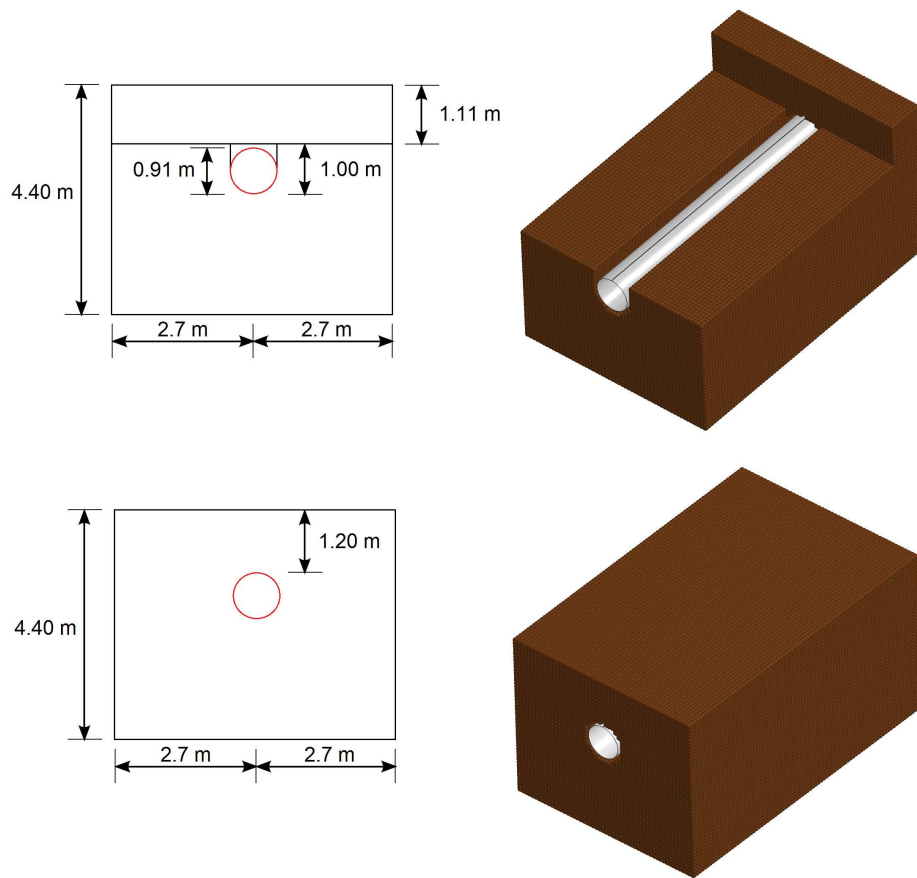$$\tau_{max} = C + \sigma_n \cdot \tan \phi, \tag{13}$$

Figure 7: The geometry of the SPH backfill representation in Test 1 (top) and Tests 2 and 3 (bottom).

Table 5: Parameters used for the backfill materials. Tests 1 and 3 correspond to clay and Test 2 corresponds to silt. G is the elastic shear modulus, ν is Poisson's ratio, ϕ is the friction angle, C is the cohesion and ψ is the dilatation angle.

Test	Density (kg m^{-3})	G (MPa)	ν	ϕ (deg)	C (kPa)	ψ (deg)
1 and 3	1900	14.8	0.35	25	8.0	0.0
2	1750	3.8	0.30	35	2.0	5.0

where τ_{max} is the maximum shear stress on any plane, σ_n is the normal stress on that plane and is positive in compression, C is the cohesion and ϕ is the angle of internal friction. The increment in equivalent plastic strain tensor, $d\boldsymbol{p}$, is calculated as

$$d\boldsymbol{p} = d\lambda \frac{\partial g}{\partial \boldsymbol{\sigma}}, \tag{14}$$

where $d\lambda$ is the incremental plastic multiplier, and g is the plastic flow potential of the MC model given by

$$g(\sigma_I, \sigma_{III}) = \frac{1 + \sin(\psi)}{1 - \sin(\psi)} \sigma_I - \sigma_{III} + K, \tag{15}$$

where σ_I and σ_{III} are the maximum and minimum principal stresses, respectively, ψ is the dilatation angle and K is a constant. The material parameters used in the MC model are taken as typical values for clay and silt [69]. The parameters are given in Table 5. The elastic shear modulus, the friction angle and the dilatation angle are assumed independent of plastic straining.

4. Results and discussion

4.1. Crack propagation and pressure along the pipe

Tests 1–3 (see Table 1) were simulated with the described coupled fluid-structure model. The experimentally measured crack velocities, the final crack lengths and the pressure at various axial positions [8] were compared with those obtained from the simulations. The experimental pressure and fracture velocity data points from the West-Jefferson tests were extracted digitally from Figures 12 and 13 in [8]. However, the fracture velocity of Test 3 in the West direction is not included here due to an ambiguous measurement in the experiment [8]. The experimental and simulation results in each direction of crack growth, West and East, were considered separately for each test. In all simulations, symmetry boundary conditions were enforced on one side of the model, representing the boundary between East and West. Thus, it was assumed that there were no interactions between the two directions. In Test 1, the material properties of the steel pipe and the boundary conditions were identical in the East and West directions, thus only one simulation was run for this test. For Tests 2 and 3, the material properties of the steel pipe in the East and West directions differed, so one simulation was run for each direction. The grid size for the fluid model was identical to the size of the elements along the pipe axis, i.e. about 25 mm. The simulated and experimental results are compared in Figure 8. Based on the assumptions for the steel and backfill material properties described in Section 3, the simulated crack velocities, final crack length, and pressure at various axial positions [8] are generally in good agreement with those obtained in the experiments.

In Test 1, the crack propagated approximately 1.0 m before it rang off and arrested at the bottom of the pipe. A very similar crack path was observed in both directions. The total length of the crack path in one direction, including ring-off, is estimated to be 2.4 m based on Figure 15 in [8]. The simulation model predicted crack arrest after 3.5 m propagation in the longitudinal direction of the pipe. In the model, ring-off is not accounted for. Nevertheless, the model captured the main feature of the crack propagation; the crack arrested shortly after initiation. From the comparison between experimental and simulated pressure in Figure 8b, it can be observed that the pressure plateau is overestimated by 5–10 bar by the model, though a more definite estimate is clouded by the noise in the experimental data. The pressure decay from the initial pressure down to the pressure plateau seems to have a steeper gradient in the experiments than in the simulations.

In Test 2, the crack propagated approximately 1.3 m in both directions before it rang off. The opening angle of the flap in this test was not as large as in Test 1, and the total crack length in each direction is estimated to be approximately 1.8 m based on Figure 16 in [8]. In the simulations, the crack length in both directions was about

1.8 m, but again, since the numerical model does not take ring-off into account, the simulation overestimated the longitudinal component of the crack path, in this case by approximately 0.5 m. In Tests 1 and 2, due to the absence of timing wires in the first 0.25 m of propagation, the initial fracture velocity is unknown. However, from the measured results in Figure 8c, it cannot be ruled out that the initial fracture velocity in the first 0.25 m was higher than the maximum velocity measured, i.e., 50–60 m s^{-1}. Thus the agreement between the model and the experiment is deemed to be good. As in Test 1, the pressure plateau was slightly overpredicted by the model.

In Test 3, the fracture-velocity readings in the West direction were disturbed in the experiment, but the overall results indicated that the crack propagation was similar in both directions. Crack arrest took place after the fracture had propagated, in both directions, through the test section (MAT4 and MAT5) and about 2.5 m into the high-toughness end pipes (MAT6). In the simulations, the crack propagation was nearly identical in the East and West directions, and the simulated fracture velocity was slightly lower than the experimentally measured velocity in the range 1–4 m. As can be seen from Figure 8e, the crack-propagation velocity was significantly reduced when the crack passed from MAT4 and MAT5 into MAT6. This is due to the more ductile behaviour of MAT6. An excellent agreement between the simulations and the experiment was obtained for the pressure seen in Figure 8f. In particular, an almost perfect match with the measured plateau pressure was obtained in the simulations. It is noted that a correction has been made for 'time zero' in Figure 8f. Based on the speed of sound in the fluid at the initial condition (i.e. 430 m s^{-1}) and the distance from the edge of the cutter to the first pressure sensor, we found that the 'time zero' of Test 3 was 16 ms later than what was reported in [8].

The experimental and simulated plateau pressures seen in Figure 8f are about 90 bar. This can be compared with the 'ideal' plateau pressure seen in Figure 6b. It should be noted, however, that the simulated plateau pressure in Figure 8f is a saturation pressure (see the phase diagram in Figure 6a) due to the equilibrium assumption, while the measured plateau pressure is not necessarily an equilibrium pressure. The simulation in Figure 8f and the plot in Figure 6b are generated using the Peng–Robinson EOS. The EOS-CG, which is expected to be more accurate, yields a saturation pressure of 93.2 bar in this case, see Table 1. Thus, if we had implemented a more accurate EOS in the coupled fluid-structure model, we would, paradoxically, have obtained a plateau pressure of 93.2 bar and a larger deviation with the experimental results for Test 3. One way of reducing the simulated pressure could be to take delayed nucleation into account. Such a non-equilibrium formulation would allow the pressure to go below the saturation pressure during the first instants of the depressurization. This constitutes an interesting avenue for future work.

The correspondence between experiments and simulation results shown in Figure 8 is a the result of a complex interplay between various physical phenomena – and their modelling. To further improve the predictive capability of the coupled fluid-structure model, each submodel has to be considered individually, since one cannot necessarily infer from the comparison between crack-arrest experimental data and simulated results which submodel has the largest uncertainty. For instance, the simulations of Test 1 and Test 2 to some extent overpredicted the plateau pressure. This may stem from the structural side, i.a. the absence of the ring-off mode in the simulations, or it may be connected to the modelling of the fluid flow. However, it should be noted that the uncertainties are not only in the numerical modelling. This can be seen e.g. in Figure 8d where the measured pressure at 5.8 m on the East side (red dashed line) and West side (red dotted line) are significantly different. This is despite the pipe properties being essentially symmetric, which would imply symmetric pressure profiles.

In the following, we will discuss the effect of pressure reflections in a short pipe, and the stress and strain history in the material along the crack path.

### 4.2. Impact of the pressure-wave reflection from the pipe end cap

Cosham et al. [8] pointed out that the crack arrest in Test 3 possibly was affected by the arrival of the reflected pressure wave. Therefore, no conclusions were drawn regarding the required toughness for fracture arrest other than that it should be similar to or larger than the toughness in MAT4 and MAT5. In order to assess this issue, a new simulation of Test 3 East was run, where the fluid model was configured with non-reflecting (transmissive) boundary conditions, emulating the fluid behaviour of an infinite pipe. The results are displayed in Figure 9. As shown in Figure 9a, the crack speed as a function of crack position is insensitive to the boundary conditions up to a crack position of 5.7 m. At this point, the reflected pressure wave reaches the crack tip in the 'standard' simulation. This can be seen in Figure 9b, where the crack-tip pressures of the two simulations start to deviate at about 40 ms. In the standard simulation, the pressure at the pipe walls behind the crack tip starts to decrease, which leads to lower crack velocity
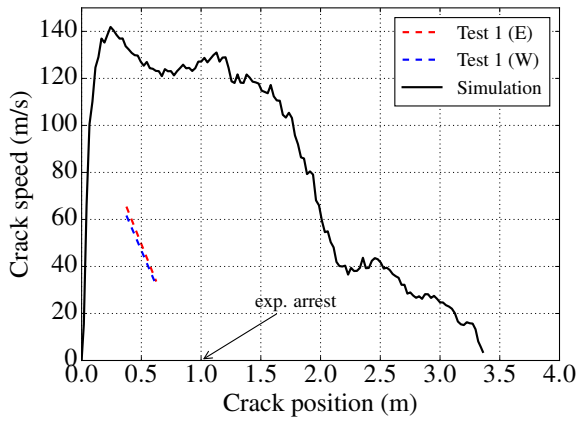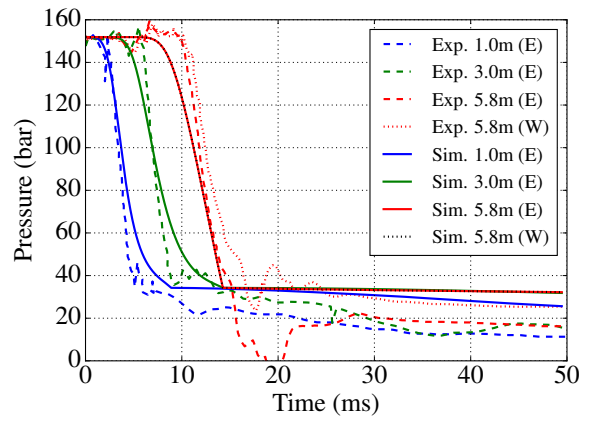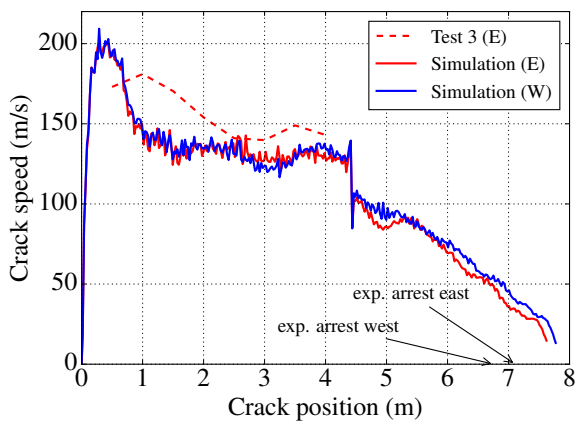
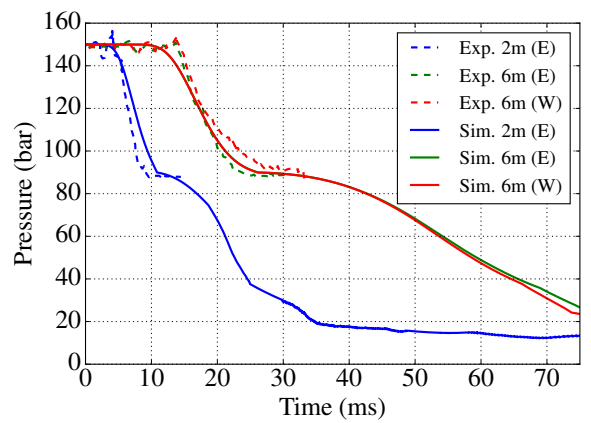(a) Test 1: Crack speed.
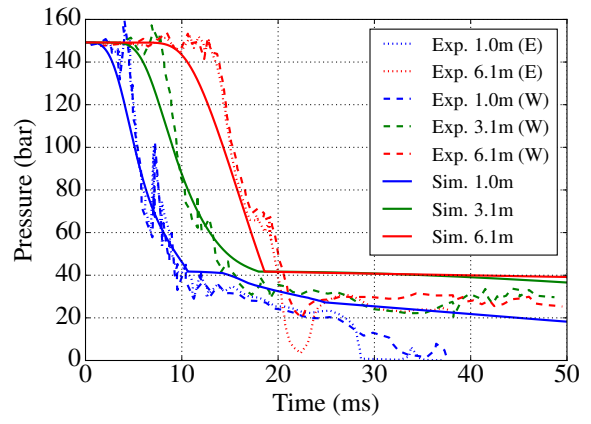
(b) Test 1: Pressure history.
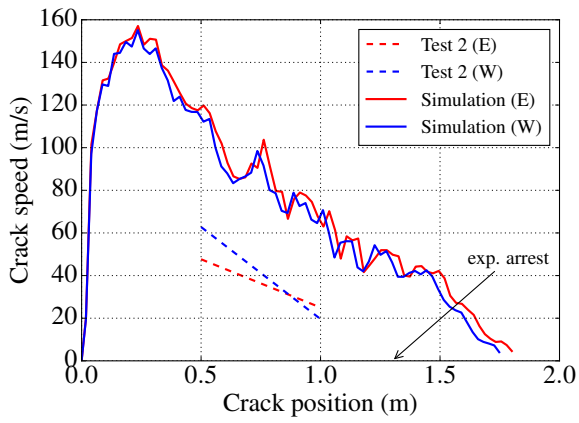
(c) Test 2: Crack speed.

(d) Test 2: Pressure history.

(e) Test 3: Crack speed.

(f) Test 3: Pressure history.

Figure 8: Comparison between experimental and simulation results.

17

and eventually arrest. In the simulation with a non-reflecting boundary, the crack propagates further and eventually tears the whole pipe in two.

As can be seen from Figure 9a, the crack speed is steadily decreasing during the last part of the propagation in both cases, thus a longer pipe with MAT6 might have been able to arrest the RDF. In the full-scale experiments presented by Cosham et al. [9], crack arrest was observed in pipes with similar toughness as MAT6. However, the plateau pressure, and so the crack-driving force in these tests, were somewhat lower than in the West-Jefferson Test 3. In conclusion, the toughness needed to arrest a crack under the conditions in Test 3 is not entirely clear from this numerical study, but the crack arrest observed at around 7 m in the West-Jefferson experiments (Test 3 East and Test 3 West) is likely to be a result of the reflected pressure wave.

The effect of the boundary conditions on the pressure wave is further illustrated in Figure 9c. Here we consider a full-bore depressurization from the left-hand end of a pipe without a propagating crack. In case of non-reflecting (NR) boundary conditions, the rarefaction wave is simply propagating to the right. For the reflecting (R) boundary conditions, the rarefaction wave is reflected at the pipe end cap at the right-hand side and it then travels to the left. As a result of this, the pressure-plateau level is reduced from 90.0 bar to 76.5 bar. It is this effect that gives the reduced load on the pipe illustrated in Figure 9b.

4.3. Deformation state prior to fracture

In order to understand the mechanical and material mechanisms at play during an RDF, a detailed analysis of the events that eventually lead to fracture is done in the following. Particular attention is put on local plastic deformation, and the stress state of the material in front of the moving crack tip prior to fracture.

The elements along the crack path had a very similar deformation mode in all simulations. In the following, the deformation of elements along the crack path in the model of Test 3 in East direction is presented. Figure 10a shows the initial rectangular geometry of all elements along the crack path, while Figures 10b and 10c show the deformed geometry at the time step before the element is deleted in selected elements along the crack path in MAT5 and MAT6, respectively. For both materials, because of the hoop stress, almost all deformation occurs in the in-plane transverse (circumferential) direction; the elongation in the crack-path direction is approximately 9%, while the average elongation in the in-plane transverse direction is 59% and 88% for MAT5 and MAT6, respectively. For the elements in the crack path, this implies a state of stress near plane-strain tension in the crack-path direction.

As can be seen from Figures 10b and 10c, the in-plane area of the elements is significantly increased during plastic deformation. Since the plastic deformation is assumed to be purely deviatoric, the thickness at fracture is reduced to approximately 14.6 mm for MAT5 and 12.4 mm for MAT6. In contrast to a solid element, the deformation in the thickness direction of a shell element is not constrained by its neighbouring elements. Thus, a shell-element mesh will predict the local necking phenomenon over a length scale corresponding to the in-plane size of the element. In the RDF simulations, a near plane-strain condition prevails in the crack-path direction, and so the size of the shell element in the in-plane transverse direction is the most significant part in the spatial discretization. If we assume that the local neck occurs over a width corresponding to the initial thickness, i.e. 25.4 mm, an initial element width of approximately half the thickness is appropriate to capture the local neck – because of an average elongation between 59% and 88% – within one element for these materials, see Figures 10b and 10c. By letting the element size be approximately equal to the thickness of the pipe in the longitudinal direction, we obtain an in-plane aspect ratio of the element at fracture that is close to unity.

The time histories of the equivalent plastic strain and the equivalent plastic strain rate were collected from selected elements along the crack path. The selected elements are positioned 0 mm, 50 mm and 4.66 m from the crack tip at the initiation of simulation step 2, i.e. RDF. The material of the former two elements is MAT5, while the material of the latter element is MAT6. Figure 11a shows the equivalent plastic strain versus time (p–t) curve from the selected elements. Note that the quasi-static (due to implicit analysis) loading step (step 1) was conducted over the first 6 ms, thus the elements closest to the crack tip were deformed immediately at the beginning of step 2, while the RDF took approximately 35 ms to reach the element located 4.66 m from the crack tip. Further, Figure 11a shows that the equivalent plastic strain at fracture in MAT5 is approximately 0.65, while it is approximately 0.85 in MAT6. Figure 11b shows the equivalent plastic strain rate versus time curve ($\dot{p}$–t) for the three elements. The strain rate of the element located closest to the initial crack tip peaks at approximately 1100 s^{-1}, while the element located 50 mm from the crack tip reaches a maximum $\dot{p}$ of approximately 1750 s^{-1}. The discrepancy of the maximum $\dot{p}$ value in these
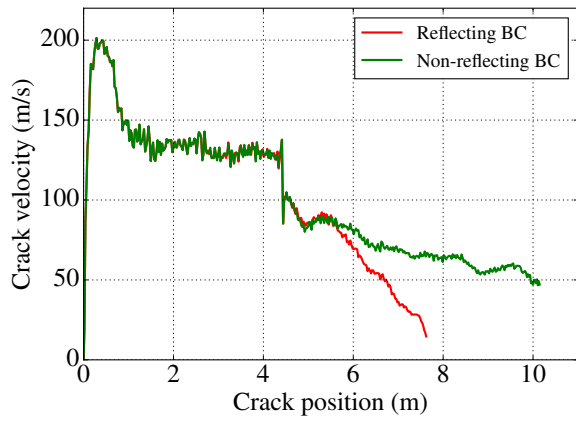
(a) Crack speed.
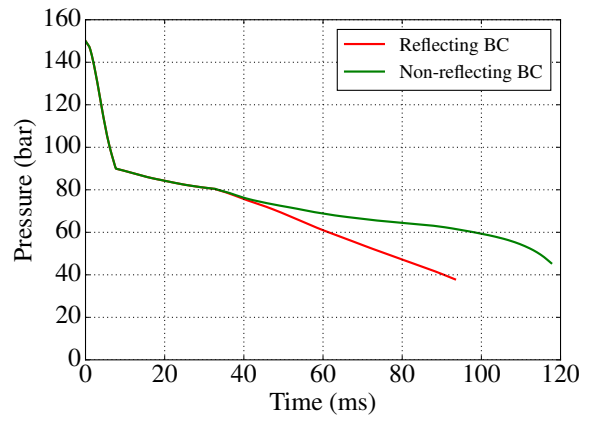
(b) Pressure at crack tip.
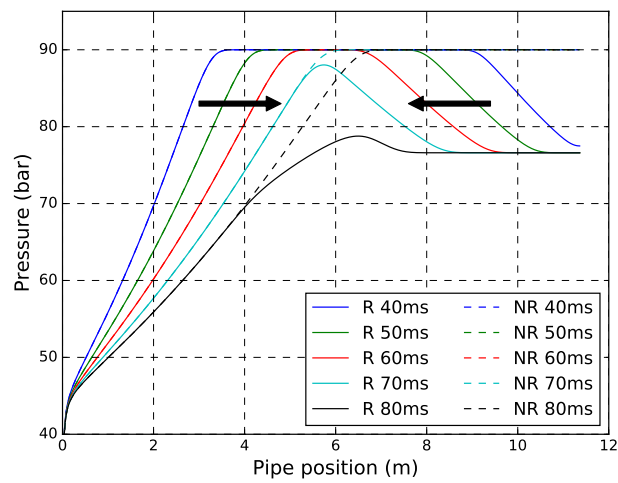
(c) Full-bore depressurization of a pipe. Effect of reflecting (R) versus
non-reflecting (NR) boundary conditions at the right-hand side.

Figure 9: Test 3. Simulation of the effect of the pipe end cap on the running-ductile fracture using reflecting and non-reflecting boundary conditions.
The pressure reflection of a short pipe gives a reduced pressure load.
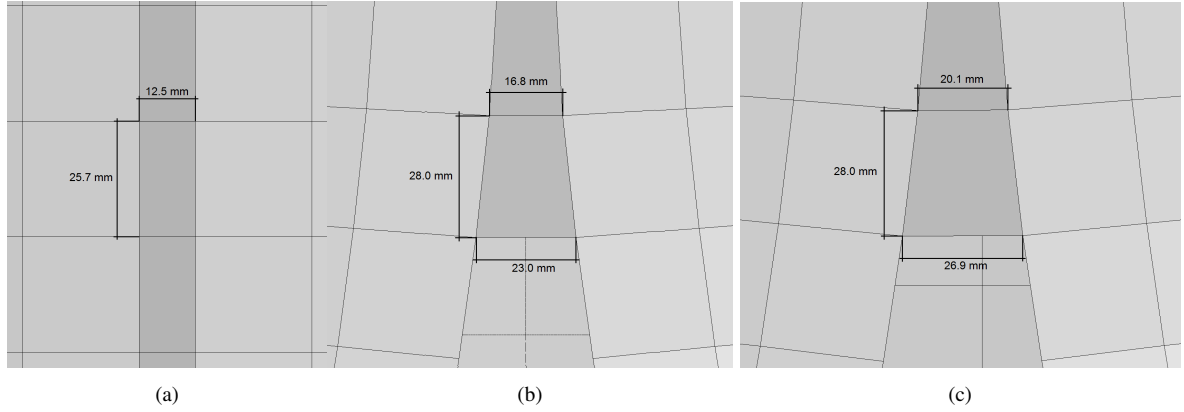
Figure 10: Shape of representative elements along crack path in simulation of Test 3 East. The initial in-plane geometry is shown in (a), while the deformed shape at the instant before element erosion is shown for MAT5 in (b) and for MAT6 in (c).
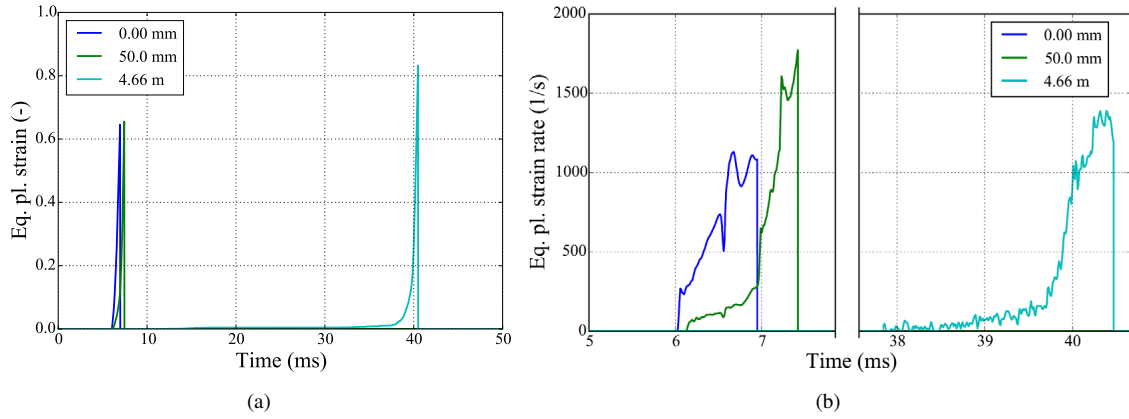

Figure 11: Time histories of (a) equivalent plastic strain, p, and (b) equivalent plastic strain rate, $\dot{p}$, from selected elements along the crack path in Test 3 East. The elements are located 0 mm, 50 mm and 4.66 m from the initial crack.

two elements may be related to inertia effects at the initiation of the crack propagation. The maximum $\dot{p}$ value in the element located 4.66 m from the crack tip is approximately $1400\,\text{s}^{-1}$. The strain rate in the elements is related to the speed of the RDF, which is lower in MAT6 than in MAT5. The elements located 50 mm and 4.66 m from the crack tip display a sudden increase in strain rate approximately 1 ms after onset of plastic deformation. This sudden increase in strain rate is likely to stem from onset of local necking in the elements.

In order to assess the stress state in the pipe prior to fracture, the histories of stress triaxiality, σ^*, Lode parameter, μ, and equivalent plastic strain, p, were collected from the selected elements along the crack path of Test 3 East. The results in terms of σ^*–p and μ–p curves are displayed in Figure 12. As can be seen from Figure 12, the element located at the crack tip (0 mm) has a stress state close to plane strain tension ($\sigma^* = \sqrt{3}/3, \mu = 0$) during the whole deformation history prior to fracture, while the other two elements start to deform in near equi-biaxial stress ($\sigma^* = 2/3, \mu = 1$) before they gradually move into a stress-state near plane-strain tension. Thus, the elongation in the crack-path direction observed in Figure 10b and Figure 10c occurs at the beginning of the plastic deformation. Eventually, onset of local necking drives all in-plane deformation in the transverse direction of the crack path and the element is deformed in a state of plane-strain tension. The CL fracture loci for MAT5 and MAT6 as estimated from Eq. (12) under the assumption of a strain rate of $\dot{p} = 1000\,\text{s}^{-1}$ are shown in Figure 12a. The predicted fracture strain from Eq. (12) assumes proportional loading, but it is in good agreement with the results from the numerical model. It is noted that the CL fracture strain estimated by Eq. (12) is proportional to $(1 + \dot{p}/\dot{p}_0)^{-C/(n+1)}$, thus, if the strain rate is changed from $\dot{p} = 0.001\,\text{s}^{-1}$ to $\dot{p} = 1000\,\text{s}^{-1}$, the fracture strain in the CL model is lowered by a factor of 0.86 for
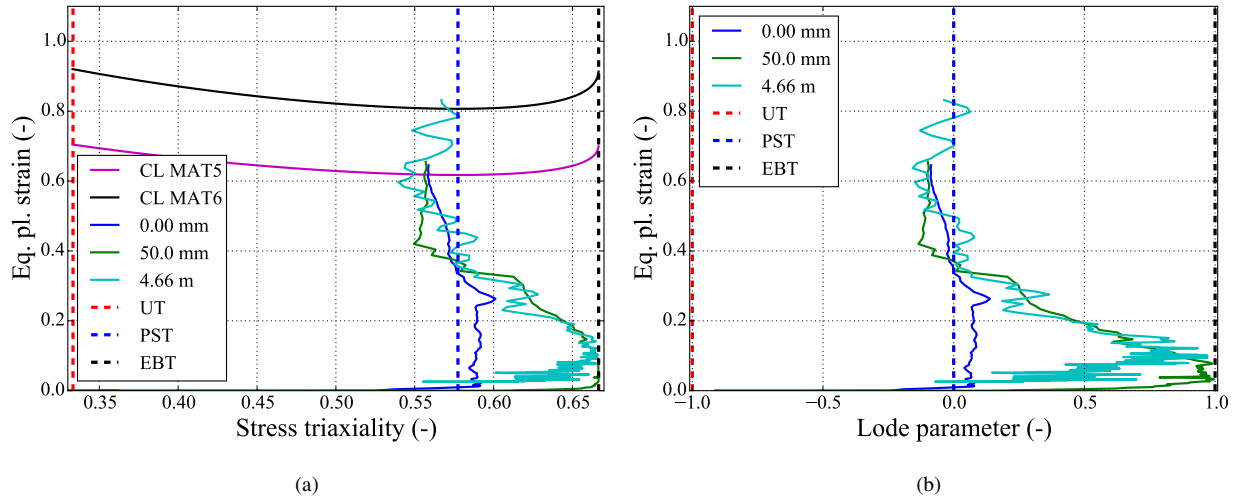
20

Figure 12: Stress and strain histories from elements along the crack path in Test 3 East. The elements are located 0 mm, 50 mm and 4.66 m from the initial crack. The two elements closest to the crack tip belong to MAT5, while the third element comes from MAT6. (a) Histories of equivalent plastic strain, p, as a function of stress triaxiality, σ^* and the CL loci for MAT5 and MAT6 following Eq. (12) assuming $\dot{p} = 1000 \, \text{s}^{-1}$. (b) Histories of equivalent plastic strain, p as function of Lode parameter, μ.

MAT5 and MAT6. Considering the large strain rates at hand in the elements along the crack path, a significant change of temperature is expected. However, adiabatic heating will reduce the strength of the material and at the same time increase the ductility. Thus, the total effect of adiabatic heating on the RDF velocity is not clear.

The above analysis shows that large plastic deformation is reached in the material in front of the crack tip prior to onset of fracture. Moreover, the stress state of the material near the crack tip is dominated by plane-strain tension before fracture occurs, independent of the crack velocity or material properties. This implies that in RDF modelling, a fracture criterion accounting for a large range of stress states is not necessary; a fracture criterion which is valid for plane-strain tension is sufficient. However, the effect of strain rate and adiabatic heating may influence the predicted results, and will be studied in future work. Finally, this analysis justifies the choice made regarding the size of the elements where fracture propagates.

5. Conclusion

In this work, we have considered a coupled fluid-structure model whose predictions of running-ductile fracture can help obtaining fracture-propagation control in CO_2-transport pipelines. The fluid flow inside the pipe, and out of the pipe through the fracture, is computed using a one-dimensional homogeneous equilibrium model. The thermodynamic properties of pure CO_2 are calculated with the Span–Wagner equation of state (EOS), while those of CO_2-rich mixtures are calculated using the Peng–Robinson EOS. The backfill, i.e. the soil material surrounding the pipe, is modelled by SPH particles employing the Mohr-Coulomb constitutive model. The pipe is represented by shell elements with an in-plane size close to the thickness of the pipe. The steel is described by the visco-plastic J_2 constitutive equation and the Cockroft–Latham fracture criterion. Due to limited available experimental material data, a novel calibration procedure is developed to determine the work-hardening and ductility of the steel pipes. The procedure is based on existing empirical methods and reverse modelling.

Coupled-model predictions have been compared with experimental data for three reduced-length (West-Jefferson type) crack-arrest experiments with modern high-toughness pipes. Two of the tests were done with pure CO_2 and one with a CO_2-N_2 mixture. All pipes were of grade X65, 914 mm (36") diameter, wall thickness 25.4 mm and Charpy energies in the range 180–340 J. Good agreement between model predictions and experimental data was observed for the pressure along the pipes. The crack velocities were overestimated in the tests done with pure CO_2 while very good agreement was obtained for the third test with a CO_2-N_2 mixture. The model gave conservative estimates of the final arrested fracture lengths in all three tests.

The effect of the pipe end cap was simulated for the third test. The results indicate that the reflected pressure wave from the end cap represents a significant pressure drop, which is likely to have contributed to the crack arrest observed in the experiment.

A detailed analysis of the local plastic deformation in front of the crack tip was carried out. It was found that the stress state of the material was dominated by plane-strain tension before fracture occurred, implying that a fracture criterion which is valid for plane-strain tension is sufficient for numerical RDF predictions.

Finally, it is our aim in the future to employ the present model framework to develop engineering tools for fracture-propagation control in CO_2-transport pipelines. We will also seek to obtain a better understanding of the ring-off phenomenon and the plateau pressure.

Acknowledgements

References

[1] International Energy Agency (IEA), Energy Technology Perspectives 2014, IEA, 2014. doi:10.1787/energy_tech-2014-en.

[2] P. Aursand, M. Hammer, S. T. Munkejord, Ø. Wilhelmsen, Pipeline transport of CO_2 mixtures: Models for transient simulation, International Journal of Greenhouse Gas Control 15 (2013) 174–185. doi:10.1016/j.ijggc.2013.02.012.

[3] E. Aursand, S. Dumoulin, M. Hammer, H. I. Lange, A. Morin, S. T. Munkejord, H. O. Nordhagen, Fracture propagation control in CO_2 pipelines: Validation of a coupled fluid-structure model, Engineering Structures 123 (2016) 192–212. doi:10.1016/j.engstruct.2016.05.012.

[4] W. A. Maxey, Fracture initiation, propagation and arrest, in: Fifth Symposium on Line Pipe Research, American Gas Association, Houston, Texas, USA, 1974, pp. J1–J31.

[5] R. Cooper, National Grid's COOLTRANS research programme, Journal of Pipeline Engineering 11 (3) (2012).

[6] J. Barnett, R. Cooper, The COOLTRANS research programme: Learning for the design of CO_2 pipelines, in: 10th International Pipeline Conference, IPC 2014, American Society of Mechanical Engineers, 2014. doi:10.1115/ipc2014-33370.

[7] D. G. Jones, A. Cosham, K. Armstrong, J. Barnett, R. Cooper, Fracture-propagation control in dense-phase CO_2 pipelines, in: 6th International Pipeline Technology Conference, Tiratsoo Technical, Ostend, Belgium, 2013, pp. 7–9, paper S06-02.

[8] A. Cosham, D. G. Jones, K. Armstrong, D. Allason, J. Barnett, Ruptures in gas pipelines, liquid pipelines and dense phase carbon dioxide pipelines, in: 9th International Pipeline Conference, IPC 2012, American Society of Mechanical Engineers, 2012, pp. 465–482. doi:10.1115/ipc2012-90463.

[9] A. Cosham, D. G. Jones, K. Armstrong, D. Allason, J. Barnett, Analysis of two dense phase carbon dioxide full-scale fracture propagation tests, in: 10th International Pipeline Conference, IPC 2014, Vol. 3, American Society of Mechanical Engineers, Calgary, Canada, 2014. doi:10.1115/IPC2014-33080.

[10] Anon, Petroleum and natural gas industries – Pipeline transportation systems, BS 14161:2011, British Standards Institution, London, UK (2011).

[11] Anon, Pipeline transportation systems for liquids and slurries, ASME code for pressure piping, B31, ASME B31.4, American Society of Mechanical Engineers, New York, USA (2012).

[12] G. Wilkowski, D. Rudland, H. Xu, N. Sanderson, Effect of grade on ductile fracture arrest criteria for gas pipelines, ASME Conference Proceedings 2006 (42630) (2006) 369–384. doi:10.1115/ipc2006-10350.

[13] G. Wilkowski, D.-J. Shim, Y. Hioe, S. Kalyanam, F. Brust, How new vintage line pipe steel fracture properties differ from old vintage line pipe steels, in: 9th International Pipeline Conference, IPC 2012, ASME, Calgary, Canada, 2012. doi:10.1115/ipc2012-90518.

[14] B. N. Leis, X.-K. Zhu, T. P. Forte, E. B. Clark, Modeling running fracture in pipelines – Past, present, and plausible future directions, in: 11th International Conference on Fracture, ICF11, Vol. 8, 2005, pp. 5759–5764.

[15] A. Cosham, The saturation pressure and the design of dense-phase carbon dioxide pipelines, in: The Third International Forum on the Transportation of CO_2 by Pipeline, Clarion Technical Conferences, Gateshead, UK, 2012.

[16] L. B. Freund, D. M. Parks, Analytical Interpretation of Running Ductile Fracture Experiments in Gas-pressurized pipelines, American Society for Testing and Materials, 1980, pp. 359–378. doi:10.1520/stp27457s.

[17] NETL, CO_2 impurity design parameters, Tech. Rep. DOE/NETL-341-011212, National Energy Technology Laboratory, USA (Aug. 2013). URL http://www.netl.doe.gov/File%20Library/Research/Energy%20Analysis/Publications/QGESS_CO2Purity_Rev3_20130927_1.pdf

[18] S. T. Munkejord, M. Hammer, S. W. Løvseth, CO_2 transport: Data and models – A review, Applied Energy 169 (2016) 499–523. doi:10.1016/j.apenergy.2016.01.100.

[19] E. Aursand, C. Dørum, M. Hammer, A. Morin, S. T. Munkejord, H. O. Nordhagen, CO_2 pipeline integrity: Comparison of a coupled fluid-structure model and uncoupled two-curve methods, in: N. Røkke, H. Svendsen (Eds.), 7th Trondheim Conference on CO_2 Capture, Transport and Storage (TCCS-7), BIGCCS / SINTEF / NTNU, Energy Procedia, vol. 51, Trondheim, Norway, 2014, pp. 382–391. doi:10.1016/j.egypro.2014.07.045.

[20] H. Mahgerefteh, S. Brown, G. Denton, Modelling the impact of stream impurities on ductile fractures in CO_2 pipelines, Chemical Engineering Science 74 (2012) 200–210. doi:10.1016/j.ces.2012.02.037.

[21] I. Scheider, A. Nonn, A. Völling, A. Mondry, C. Kalwa, A damage mechanics based evaluation of dynamic fracture resistance in gas pipelines, Procedia Materials Science 3 (0) (2014) 1956–1964. doi:10.1016/j.mspro.2014.06.315.

[22] M. F. Kanninen, P. E. O'Donoghue, Research challenges arising from current and potential applications of dynamic fracture mechanics to the integrity of engineering structures, International Journal of Solids and Structures 32 (17) (1995) 2423–2445. doi:10.1016/0020-7683(94)00275-2.

[23] D.-J. Shim, G. Wilkowski, D. Rudland, B. Rothwell, J. Merritt, Numerical simulation of dynamic ductile fracture propagation using cohesive zone modeling, in: 2008 7th International Pipeline Conference, American Society of Mechanical Engineers, 2008, pp. 21–28. doi:10.1115/ipc2008-64049.

[24] X.-K. Zhu, Existing methods in ductile fracture propagation control for high-strength gas transmission pipelines, in: ASME Pressure Vessels and Piping Conference, Vol. 6B, American Society of Mechanical Engineers, Paris, France, 2013. doi:10.1115/PVP2013-98052.

[25] H. Nakai, K. Shibanuma, S. Aihara, Numerical model for unstable ductile crack propagation and arrest in pipelines using finite difference method, Engineering Fracture Mechanics 162 (2016) 179–192. doi:10.1016/j.engfracmech.2016.03.048.

[26] A. Volling, M. Erdelen-Peppler, C. Kalwa, H. Brauer, B. Ouaissa, H. Meuser, Numerical approach for crack-arrest prediction by FEM, in: 6th International Pipeline Technology Conference, 2013, pp. S19–01.

[27] R. H. Talemi, S. Brown, S. Martynov, H. Mahgerefteh, Hybrid fluid-structure interaction modelling of dynamic brittle fracture in steel pipelines transporting CO_2 streams, International Journal of Greenhouse Gas Control 54 (2) (2016) 702–715. doi:10.1016/j.ijggc.2016.08.021.

[28] T. Berstad, C. Dørum, J. P. Jakobsen, S. Kragset, H. Li, H. Lund, A. Morin, S. T. Munkejord, M. J. Mølnvik, H. O. Nordhagen, E. Østby, CO_2 pipeline integrity: A new evaluation methodology, in: J. Gale, C. Hendriks, W. Turkenberg (Eds.), GHGT-10 – 10th International Conference on Greenhouse Gas Control Technologies, IEAGHGT, Energy Procedia vol. 4, Amsterdam, The Netherlands, 2011, pp. 3000–3007. doi:10.1016/j.egypro.2011.02.210.

[29] H. O. Nordhagen, S. Kragset, T. Berstad, A. Morin, C. Dørum, S. T. Munkejord, A new coupled fluid-structure modelling methodology for running ductile fracture, Computers & Structures 94–95 (2012) 13–21. doi:10.1016/j.compstruc.2012.01.004.

[30] K. E. T. Giljarhus, S. T. Munkejord, G. Skaugen, Solution of the Span-Wagner equation of state using a density-energy state function for fluid-dynamic simulation of carbon dioxide, Industrial & Engineering Chemistry Research 51 (2) (2012) 1006–1014. doi:10.1021/ie201748a.

[31] M. Hammer, Å. Ervik, S. T. Munkejord, Method using a density-energy state function with a reference equation of state for fluid-dynamics simulation of vapor-liquid-solid carbon dioxide, Industrial & Engineering Chemistry Research 52 (29) (2013) 9965–9978. doi:10.1021/ie303516m.

[32] E. Aursand, P. Aursand, T. Berstad, C. Dørum, M. Hammer, S. T. Munkejord, H. O. Nordhagen, CO_2 pipeline integrity: A coupled fluid-structure model using a reference equation of state for CO_2, in: T. Dixon, K. Yamaji (Eds.), GHGT-11 – 11th International Conference on Greenhouse Gas Control Technologies, RITE / IEAGHGT, Energy Procedia, vol. 37, Kyoto, Japan, 2013, pp. 3113–3122. doi:10.1016/j.egypro.2013.06.197.

[33] J. Gernert, R. Span, EOS-CG: A Helmholtz energy mixture model for humid gases and CCS mixtures, Journal of Chemical Thermodynamics 93 (2016) 274–293. doi:10.1016/j.jct.2015.05.015.

[34] A. Cosham, personal communication.

[35] J. O. Hallquist, LS-DYNA Keyword User's Manual, Livermore Software Technology Corporation (2007).

[36] K. L. Nielsen, J. W. Hutchinson, Cohesive traction-separation laws for tearing of ductile metal plates, International Journal of Impact Engineering 48 (SI) (2011) 15–23. doi:10.1016/j.ijimpeng.2011.02.009.

[37] A. Arabei, I. Pyshmintsev, M. Shtremel, A. Glebov, A. Struin, A. Gervasev, Resistance of X80 steel to ductile-crack propagation in major gas lines, Steel in Translation 39 (9) (2009) 719–724. doi:10.3103/s0967091209090010.

[38] E. Voce, The relationship between stress and strain for homogeneous deformation, Journal of the Institute of Metals 74 (1948) 537–562.

[39] T. Børvik, B. T. Hopperstad, O. S., M. Langseth, A computational model of viscoplasticity and ductile damage for impact and penetration, European Journal of Mechanics - A/Solids 20 (2001) 685–712. doi:10.1016/S0997-7538(01)01157-3.

[40] T. Belytschko, W. Liu, B. Moran, Nonlinear Finite Elements for Continua and Structures, Wiley Chichester, 2000.

[41] G. Gruben, O. S. Hopperstad, T. Børvik, Simulation of ductile crack propagation in dual-phase steel, International Journal of Fracture 180 (2013) 1–22. doi:10.1007/s10704-012-9791-2.

[42] G. Gruben, M. Langseth, E. Fagerholt, O. S. Hopperstad, Low-velocity impact on high-strength steel sheets: An experimental and numerical study, International Journal of Impact Engineering 88 (2016) 153–171. doi:10.1016/j.ijimpeng.2015.10.001.

[43] M. G. Cockcroft, D. J. Latham, Ductility and the workability of metals, Journal of the Institute of Metals 96 (1968) 33–39.

[44] A. Liessem, G. Knauf, S. Zimmermann, Strain based design -what the contribution of a pipe manufacturer can be, in: Proceedings of the Seventeenth (2007) International Offshore and Polar Engineering Conference, 2007.

[45] C. Lu, G. Michal, P. Venton, A new fracture velocity model for high grade gas pipelines, in: 20th Joint Technical Meeting on Pipeline Research, 2015.

[46] A. Cosham, D. G. Jones, B. N. Leis, P. Hopkins, J. Barnett, Not another charpy v-notch correction factor. . . ?, in: Proceedings of the 6th International Pipeline Technology Conference, Paper, 2013.

[47] Dassault Systèmes, Abaqus Theory Guide (2014).

[48] F. A. McClintock, A criterion for ductile fracture by the growth of holes, J. Appl. Mech. 35 (2) (1968) 363–371. doi:10.1115/1.3601204.

[49] J. Rice, D. M. Tracey, On the ductile enlargement of voids in triaxial stress fields, Journal of the Mechanics and Physics of Solids 17 (3) (1969) 201–217. doi:10.1016/0022-5096(69)90033-7.

[50] Y. Bao, T. Wierzbicki, On fracture locus in the equivalent strain and stress triaxiality space, International Journal of Mechanical Sciences 46 (2004) 81–98. doi:10.1016/j.ijmecsci.2004.02.006.

[51] X. Gao, J. Kim, Modeling of ductile fracture: Significance of void coalescence, International Journal of Solids and Structures 43 (2006) 6277–6293. doi:10.1016/j.ijsolstr.2005.08.008.

[52] I. Barsoum, J. Faleskog, Rupture mechanisms in combined tension and shear experiments, International Journal of Solids and Structures 44 (2007) 1768–1786. doi:10.1016/j.ijsolstr.2006.09.031.

[53] D. Mohr, F. Ebnoether, Plasticity and fracture of martensitic boron steel under plane stress conditions, International Journal of Solids and Structures 46 (20) (2009) 3535–3547. doi:10.1016/j.ijsolstr.2009.05.011.

[54] M. Dunand, D. Mohr, Hybrid experimental-numerical analysis of basic ductile fracture experiments for sheet metals, International Journal of Solids and Structures 47 (2010) 1130–1143. doi:10.1016/j.ijsolstr.2009.12.011.

[55] G. Gruben, D. Vysochinskiy, T. Coudert, A. Reyes, O.-G. Lademo, Determination of ductile fracture parameters of a dual-phase steel by optical measurements, Strain 49 (2013) 221–232. doi:10.1111/str.12030.

[56] R. Span, W. Wagner, A new equation of state for carbon dioxide covering the fluid region from the triple-point temperature to 1100 K at pressures up to 800 MPa, Journal of Physical and Chemical Reference Data 25 (6) (1996) 1509–1596. doi:10.1063/1.555991.

[57] D. Y. Peng, D. B. Robinson, A new two-constant equation of state, Industrial & Engineering Chemistry Fundamentals 15 (1) (1976) 59–64. doi:10.1021/i160057a011.

[58] S. T. Munkejord, M. Hammer, Depressurization of CO_2-rich mixtures in pipes: Two-phase flow modelling and comparison with experiments, International Journal of Greenhouse Gas Control 37 (2015) 398–411. doi:10.1016/j.ijggc.2015.03.029.

[59] A. Jäger, R. Span, Equation of state for solid carbon dioxide based on the Gibbs free energy, Journal of Chemical and Engineering Data 57 (2) (2012) 590–597. doi:10.1021/je2011677.

[60] G. Hou, J. Wang, A. Layton, Numerical methods for fluid-structure interaction: a review, Communications in Computational Physics 12 (2) (2012) 337–377. doi:10.4208/cicp.291210.290411s.

[61] P. E. O'Donoghue, M. F. Kanninen, C. P. Leung, G. Demofonti, S. Venzi, The development and validation of a dynamic fracture propagation model for gas transmission pipelines, International Journal of Pressure Vessels and Piping 70 (1) (1997) 11–25. doi:10.1016/s0308-0161(96)00012-9.

[62] K. D. Ives, A. K. Shoemaker, R. F. McCartney, Pipe deformation during a running shear fracture in line pipe, Journal of engineering materials and technology 96 (4) (1974) 309–317. doi:10.1115/1.3443246.

[63] G. Berardo, P. Salvini, G. Mannucci, G .and Demofonti, On longitudinal propagation of a ductile fracture in a buried gas pipeline: numerical and experimental analysis, in: Proceedings of the 2000 International Pipeline Conference, Vol. 1, 2000, pp. 287–294.

[64] D. Rudland, G. Wilkowski, Effects of backfill soil properties and pipe grade on ductile fracture arrest, in: Proceedings of the 16th Biennial PRCI/EPRG/APIA Joint Technical Meeting on Pipeline Research, 2007, pp. 16–19.

[65] D. Rudland, G. Wilkowski, B. Rothwell, The effects of soil properties on the fracture speeds of propagating axial cracks in line pipe steels, in: 6th Biennial International Pipeline Conference, IPC, Vol. 3 PART A, ASME, Calgary, Canada, 2006, pp. 73–82. doi:10.1115/IPC2006-10086.

[66] G. Demofonti, A. Maresca, G. Buzzichelli, Ductile fracture propagation and arrest in offshore pipelines, Applied Mechanics Reviews 41 (2) (1988) 85–95. doi:10.1115/1.3151883.

[67] W. A. Maxey, Final report on gas expansion studies: to American Gas Association, Tech. Rep. NG-18 Report No. 133, Battelle Columbus Laboratories (1983).

[68] J. J. Monaghan, Smoothed particle hydrodynamics, Reports on Progress in Physics 68 (8) (2005) 1703–1759. doi:10.1088/0034-4885/68/8/r01.

[69] J. M. R. Ortiz, J. Serra, C. Oteo, Curso Aplicado de Cimentaciones, 3rd Edition, Colegio de Arquitectos de Madrid, 1986.